TARANIS XGRE and IDEE Detection Capability of Terrestrial Gamma-Ray Flashes and Associated Electron Beams

David Sarria[1], Francois Lebrun[1,2], Pierre-Louis Blelly[3,4], Remi Chipaux[5], Philippe Laurent[1,2], Jean-Andre Sauvaud[3,4], Lubomir Prech[6], Pierre Devoto[3,4], Damien Pailot[1], Jean-Pierre Baronick[1], and Miles Lindsey-Clark[1]

[1]APC, AstroParticule et Cosmologie, Universite Paris Diderot, CNRS/IN2P3, CEA/DRF/IRFU, Observatoire de Paris, Sorbonne Paris Cite, 10 rue Alice Domont et Leonie Duquet, F-75205 Paris Cedex 13, France
[2]CEA/DRF/IRFU/Sap, Bat. 709, Orme des Merisiers, CEA-Saclay, F-91191 Gif-sur-Yvette Cedex, France.
[3]Universite de Toulouse, UPS-OMP, IRAP, Toulouse, France.
[4]CNRS, IRAP, 9 Av. colonel Roche, Toulouse, France.
[5]CEA/DRF/IRFU/SEDI, CEA-Saclay, F-91191 Gif-sur-Yvette Cedex, France.
[6]Faculty of Mathematics and Physics, Charles University, Prague, Czech Republic.

Correspondence to: David Sarria (dsarria@apc.in2p3.fr)

Abstract.

With a launch expected in 2018, the TARANIS micro-satellite is dedicated to the study of transient phenomena observed in association with thunderstorms. On-board the spacecraft, XGRE and IDEE are two instruments dedicated to study Terrestrial Gamma-ray Flashes (TGFs) and associated electron beams (TEBs). XGRE can detect electrons (energy range: 1 MeV to 10 MeV) and X/gamma-rays (energy range: 20 keV to 10 MeV), with a very high counting capability (about 10 million counts per second), and the ability to discriminate one type of particle from the other. The IDEE instrument is focused on electrons in the 80 keV to 4 MeV energy range, with the ability to estimate their pitch angles.

Monte-Carlo simulations of the TARANIS instruments, using a preliminary model of the spacecraft, allow sensitive area estimates for both instruments. It leads to an averaged effective area of 425 cm^2 for XGRE to detect X/gamma rays from TGFs, and the combination of XGRE and IDEE gives an average effective area of 255 cm^2 to detect electrons/positrons from TEBs. We then compare these performances to RHESSI, AGILE, and Fermi GBM, using performances extracted from literature for the TGF case, and with the help of Monte-Carlo simulations of their mass models for the TEB case.

Combining this data with with the help of the MC-PEPTITA Monte-Carlo simulations of TGF propagation in the atmosphere, we build a self-consistent model of the TGF and TEB detection rates of RHESSI, AGILE, and Fermi. It can then be used to estimate that TARANIS should detect about ~~225~~ 200 TGFs/year and 25 TEBs/year.

1 Introduction

Terrestrial Gamma Ray flashes (TGFs) are short ($\sim 20\ \mu$s to ~ 1 ms) X and gamma ray emissions associated with lightning and mostly detected from space. Together with transient luminous events for the optical part (see Surkov and Hayakawa (2012) for a comprehensive review), they play an important role for understanding the coupling between magnetosphere-ionosphere-

atmosphere. A comprehensive review of TGFs and related studies, so called the High Energy Atmospheric Physics, is provided by Dwyer et al. (2012). Detections of TGFs from space were first presented by Fishman et al. (1994), using data from the the Burst And Transient Source Experiment (BATSE) on-board the NASA's Compton Gamma-Ray Observatory. In the subsequent years, TGFs were also detected from space by other satellites : the Reuven Ramaty High Energy Solar Spectroscopic Imager (RHESSI) (Smith et al., 2005), the Astro-rivelatore Gamma a Immagini Leggero (AGILE) ~~(?)~~ (Marisaldi et al., 2014) and the Fermi space telescope (Briggs et al., 2010). Very recently, TGF events were also found in the BeppoSAX data archive (Ursi et al., 2017) .

A careful analysis of BATSE, RHESSI and Fermi-GBM data permitted to identify some longer events, with durations longer than 1 ms (Smith et al., 2006; Dwyer et al., 2008; Cohen et al., 2010; Briggs et al., 2011). These events were not directly due to the detection of gamma-rays, but to secondary electrons and positrons produced by the TGF, and were called Terrestrial Electron Beams (TEBs). Contrary to gamma-rays, the charged particles are beamed by the magnetic field of the Earth, and can travel thousands of kilometers between one hemisphere to the other and may be detected in unusual locations for TGFs; e.g. the Fermi 091214 event detected above the Egyptian desert (Briggs et al., 2011; Sarria et al., 2016). These electrons/positrons can then be trapped by the geomagnetic field and they may provide a significant source of high-energy (> 1 MeV) particles to the radiation belts. The impact of TEBs on radiation belts still needs to be quantified.

In the near future, two missions are planned whose primary objective is the TGF detection : ASIM and TARANIS. The Atmosphere-Space Interaction Monitor (ASIM) is an European Space Agency (ESA) project with scientific leadership from the Technical University of Denmark (DTU) (Neubert et al., 2006). It will embark two X/Gamma Ray detectors (MXGS-LED and MXGS-HED) coupled with optical sensors (MMIA). It will be docked on the International Space Station (ISS) in the course of 2017. The Tool for the Analysis of RAdiation from lightNIng and Sprites (TARANIS) is a micro-satellite of the French Space Agency (CNES) that will be dedicated to the study of transient events related to thunderstorm activity (Lefeuvre et al., 2009) and will be launched in 2018. All instruments on-board the TARANIS spacecraft collaborate for the transient event study. Upon alert of one instrument, all instruments can record data prior, during and after the trigger. Two instruments have been specifically designed to study TGFs and TEBs : the instrument for X-Gamma-Ray and Relativistic Electrons (XGRE) and the Instrument for Detection of Energetic Electrons (IDEE). XGRE and IDEE are two of the four instruments that have the ability to trigger all the on-board instruments.

These two instruments will be presented in section 2. In section 3 we will make a comparison of the performances of XGRE and IDEE with those of RHESSI, Fermi-GBM and AGILE-MCAL, in the context of TGFs. Finally in section 4 we build a self-consistent picture to account for the detection rates of TGF and TEB seen by the satellites flying today, in order to estimate the future detection rates of TARANIS.

2 The TARANIS XGRE and IDEE instruments

2.1 The XGRE Instrument

XGRE can detect photons in the $[20\ \mathrm{keV} - 10\ \mathrm{MeV}]$ energy range and electrons in the $[1\ \mathrm{MeV} - 10\ \mathrm{MeV}]$ energy range. There are major differences when detecting photons (from TGF) and electrons or positrons (from TEB). Photons in this energy range always have a probability of not interacting with a given material, whereas an electron crossing a given material always deposits energy in it. A significant increase in photon energy always implies a significant increase in the average energy deposit on the detection material, allowing a proper estimate of the incident photon energy spectrum. The XGRE instrument also has the ability to trigger the other instruments of the TARANIS payload.

In general, the energy of an incident electron is difficult to estimate properly. Using several layers of detectors helps a lot but there remain uncertainties due to the detector's environment. Positrons will behave very similarly to electrons, with the addition that they will always annihilate into two 511 keV photons once they have lost most of their kinetic energy.

The XGRE instrument is presented in Figure 1. Figure 1.~~A. show~~ a. shows its position on the TARANIS satellite (highlighted in red). XGRE is composed of three sensors, that are tilted by 20^o with regard to the payload baseplate. The relative counts of the three sensors allow to estimate the direction of the gamma-ray flux for bright events (more than 100 counts). Simulations show that the angular resolution is about 38^o for a TGF that produces 100 counts, 27^o for 200 counts and 18^o for 400 counts. However these estimations have yet to be confirmed using measurements of the satellite calibration campaign (expected in 2018). Each sensor contains four Detection Units, as presented in Figure 1.b. . Each unit has one 8.7 mm thick lanthanum bromide crystal ($LaBr_3$) scintillator, surrounded by two 5 mm thick plastic scintillators, as shown in Figure 1.c., and the three scintillators are connected to two multi-anode photo-multipliers. This sandwich design allows the identification of the triggering photon or charged particle.

The plastic scintillators have a low effective atomic number (~~$Z \approx 6$~~$Z \approx 12$) and a low density ($1.03\ \mathrm{g/cm^3}$), therefore gamma-rays have a small probability to interact with it and/or to deposit all of their energy. On the other hand, gamma-rays have a much higher probability of interacting with the $LaBr_3$ due to its high effective atomic number ($Z = 46.9$), its five times higher density ($5.08\ \mathrm{g/cm^3}$) and its larger thickness. The three scintillators are sensitive to charged particles. If a significant amount of energy is deposited in the $LaBr_3$ only, it will probably be due to a gamma-ray. If some energy is deposited in a plastic only, it will likely be due to an electron with energy below 1.2 MeV. If energy is deposited in one (or two) plastic(s) and in a $LaBr_3$ crystal, it will likely be due to a higher energy electron (above 1.2 MeV).

The effective area of XGRE for detecting gamma-rays could be determined using ~~our~~ the GEANT4 full mass model of the instrument and satellite. GEANT4 is a toolkit developped by a international collaboration ~~lead by CERN~~led by CERN, to simulate the propagation of particles though matter (Agostinelli et al., 2003; Allison et al., 2006) . It is an essential tool to simulate high energy particle detectors and to estimate their performance.

Two side views of the GEANT4 mass model of XGRE are presented in Figure 1.a. This mass model will be refined in the next years, using results of calibration campaigns.

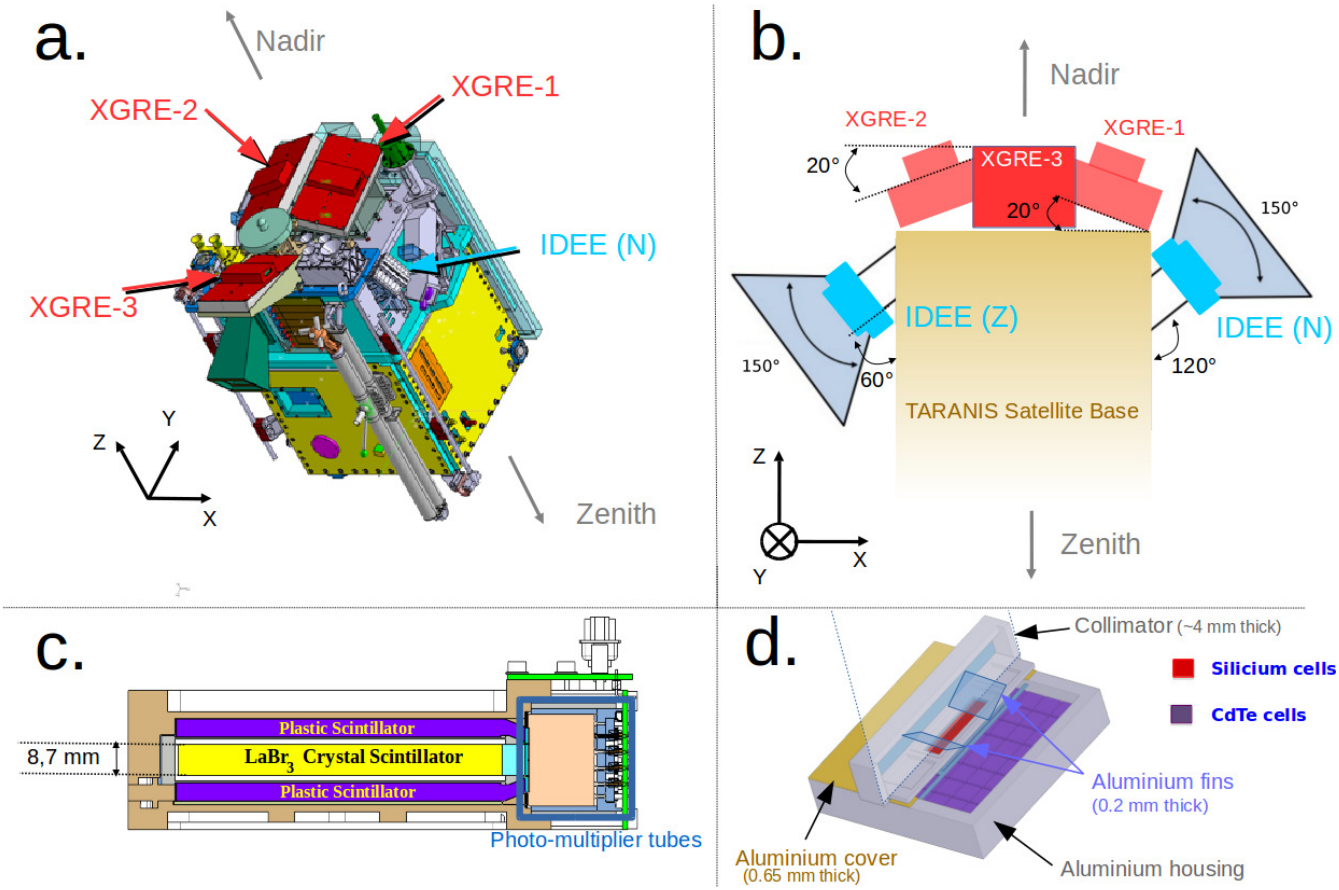

Figure 1. a. ~~Two~~ 3D view of the TARANIS spacecraft. The position of the three XGRE sensors are indicated, as well as one of the two IDEE detectors (the other is hidden). **b.** Schematic side views of the TARANIS ~~GEANT4 mass model~~spacecraft. The three XGRE sensors are highlighted in red and the two IDEE detectors are highlighted in cyan. ~~**b.** Exploded view~~ The relative positioning and orientation of ~~a XGRE sensor, showing~~ the ~~4 detectors units (brown)~~instruments are accurately represented. For more clarity, the ~~electronics and~~ relative scale of the ~~aluminium housing~~two IDEE detectors is slightly bigger than reality. **c.** Cross section view of a XGRE detector unit, highlighting the sandwich design of plastic/$LaBr_3$ scintillators. **d.** Partial cross-section view of ~~an~~ one IDEE detector's head~~, highlighting the~~ . The position of the ~~silicium~~ sensitive cells used to detect electrons (Silicium and CdTe~~cells~~) are highlighted.

To determine the response of the detector to X/gamma-rays, we drawn 150 mono-energetic beams of 20×10^6 photons, each with a different energy between 20 keV and 20 MeV. The particles are drawn from the direction of nadir, towards the satellite. Indeed, the attitude of the satellite is such that the detector will always point towards the Earth (nadir).

Any particle that deposits an energy above the electronic trigger is considered as detected, i.e. above 300 keV on a plastic scintillator and/or above 20 keV in a $LaBr_3$ crystal.

Figure 2.a. shows the computed effective area of XGRE for gamma-rays, using $LaBr_3$ (black curve). The effective area of XGRE is maximal at E_{max} ~~is about 125 keV~~(~ 125 keV) with an effective area of above 836 cm^2. Below E_{max}, the effective area decreases as weaker X-rays are more easily absorbed by materials surrounding the crystal (e.g. plastic scintillators, aluminium housing, hoods). The effective area is negligible below 20 keV by design. Above E_{max}, the effective area decreases and goes down to ≈ 190 cm^2 at 1.5 MeV. For higher energies, the pair production probability (by interaction with the detector or the surrounding material) becomes higher, increasing the effective area, that reaches ≈ 230 cm^2 at 20 MeV.

In Appendix A, we describe how we can calculate an average effective area, that is a unique value associated to a detector for detecting TGF or TEB. For the average effective area of XGRE, the calculation gives $\sigma_{XG}^{TGF} \approx 425$ cm^2 ~~. This value~~ for a TGF source located at nadir. If the TGF source is offset from nadir, the value of σ_{XG}^{TGF} goes down to 401 cm^2 (-5.6 %) for a 20^o angle, 354 cm^2 (-17 %) for 37^o, and 272 cm^2 (-36 %) for 54^o. The value of σ_{XG}^{TGF} is indicated in Table 1, together with the values for the detectors of RHESSI, Fermi and AGILE, that will be discussed in section 3.

To determine the response of the instrument to electrons (and positrons), we launch 150 mono-energetic beams of 20×10^6 electrons (or positrons), each beam with a different energy between 20 keV and 20 MeV. The electrons are drawn from two sides at 40^o from nadir and 40^o from zenith, that is representative of an average orientation of a magnetic field line seen by the satellite around equatorial regions (and this is also the orientation of the two IDEE detectors, see next section). The particles are drawn around these two directions with an uniform randomization of $\pm 30^o$ for polar an azimuthal angles.

The simulation requires for an initial particle to make a deposit of at least 300 keV on a plastic scintillator to be detected, or at least 20 keV on a $LaBr_3$ scintillator. These deposits may be due directly to the electrons, or from bremsstrahlung secondary emissions they are producing.

The effective area of XGRE against electrons is shown by the ~~blue~~ black curve of Figure 2.b. There is threshold energy E_{XG}^t of about 300 keV below which the area is very small (less than 10 cm^2). Actually, each plastic scintillator is covered by a 0.6 mm thick hood made of Polyether ether ketone (PEEK). Electrons of 1 MeV kinetic energy will deposit about E_{XG}^t in these hoods. About 10% of the area of the hood are covered by a 8 mm thick stiffener that will absorb more than ~ 3 MeV of kinetic energy from the electrons when they cross it. For energies higher than E_{XG}^t, the electrons can more likely reach the plastic scintillators because they will scatter to larger distances, and also bremsstrahlung emissions (that can be detected by the $LaBr_3$) become more and more important, increasing the effective area from $\approx$100 cm^2 at 600 keV to about 720 cm^2 at 20 MeV. Figure 2.c show the effective area of XGRE against positrons. It is essentially similar to the electron's curve, with addition of a constant value of about 280 cm^2. This constant value is due to positrons that annihilate (into two 511 keV photons) with the detector or some parts of the satellite.

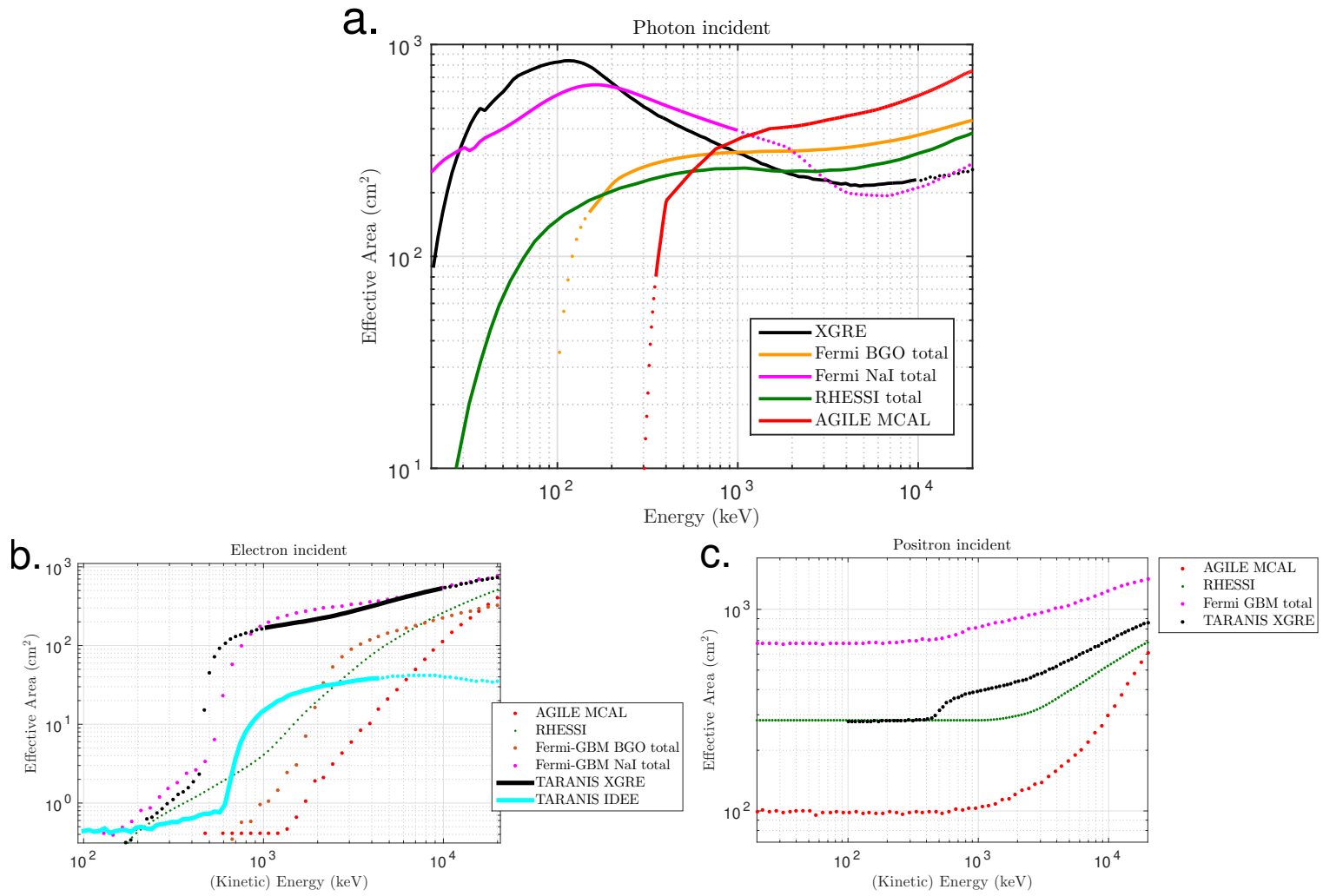

Figure 2. a. Effective area for X/gamma-rays versus energy, for the considered detectors. **b.** Effective area for electrons versus energy, for the considered detectors. **c.** Effective area for positrons versus energy, for the considered detectors.

A full line indicates that the spectroscopy is possible at the given energy, and a dot line indicates it is not.

TARANIS XGRE and IDEE data come from GEANT4 simulations performed for this work. Concerning photon response (**a.**), the data for Fermi-GBM was obtained by averaging about one hundred response matrices generated from publicly available tools provided by the Fermi-GBM collaboration. For RHESSI, the data was extracted from the response matrix provided by D. Smith. For AGILE-MCAL, this data is reproduced from literature. Concerning the response to electrons and positrons (**b.** and **c.**), these results are obtained from GEANT4 and GEANT3 simulations using the mass models of the spacecrafts (or an approximative version for Fermi). *Complete references are presented in sections 6 and 7 about code and data availability.*

To determine the effective area averaged over a TEB spectrum, σ_{XG}^{TEB}, we apply the method presented in Appendix A. The calculation gives about 233 cm^2 for XGRE. This value is presented in Table 1, together with the values obtained for the detectors of RHESSI, Fermi and AGILE, that will be discussed in section 3.

	σ^{TGF} (cm^2)	σ^{TEB} (cm^2)
RHESSI total	256[a]	74
AGILE-MCAL	220[b]	25
Fermi-GBM BGO (1 unit)	160[c]	21
Fermi-GBM NaI (1 unit)	33	14
Fermi-GBM total	716	350
XGRE	425	233
IDEE	0	22
TARANIS Total	425	255

[a] Ref : Ostgaard et al. (2012)

[b] Ref : Marisaldi et al. (2015)

[c] Ref : Briggs et al. (2013)

Table 1. Summary of the TGF-spectrum averaged (σ^{TGF}) and TEB-spectrum averaged (σ^{TEB}) effective areas of RHESSI, AGILE, Fermi and TARANIS.

2.2 The IDEE instrument

The IDEE instrument is made of two electron detectors from 80 keV to 5 MeV energy. The two main objectives of IDEE are to study Lightning-induced Electron Precipitations (LEP) (Voss et al., 1984; Inan et al., 2007), and ~~also~~ the electrons beams associated to TGFs, as known as TEBs. Two burst triggering processes run in parallel on these two type of events with different time profiles.

The spectroscopy is possible up to 4.4 MeV, and particles depositing more than this energy are counted in an overflow channel. As shown in Figure 1.d., each detector is made of 5 cells of silicium (Si) and 64 cells of cadmium telluride crystal (CdTe). The ~~disposition of the cells into two layers allows to estimate the pitch angles of the incoming charged particles, by coincidence between Si and CdTe detectors, that will provide an important complementary information to the measurements of XGRE. One detector is pointed at 30^o from nadir, and the other at 40^o from zenith. The fields of view are $150^o \times 40^o$ for the Si part and $150^o \times 150^o$ pour for the CdTe part.~~

CdTe cells are mounted in 8 rows by 8 cells format. The are four Si cells of 1 cm^2 each plus one narrow cell of 0.1 cm^2 in the center. The narrow cell is used in regions of high electron fluxes (SAA) where others cells will be disabled, to decrease significantly the geometrical factor of the sensor. The Silicium cells have a total geometrical area of 8 cm^2 (4 cm^2 per detector),

and are 0.3 mm thick. The CdTe cells are 5 mm thick and have a total geometrical area of 128 cm^2 for the sum of the two IDEE detectors, ~~therefore~~ hence most of the effective area will be due to the CdTe cells.

The two IDEE detection units are pointing 60^o from nadir (IDEE-N) and 60^o from zenith (IDEE-Z) as shown in Figure 1.b. . The designed viewing angles are 150^o x 150^o for electron energies $\geq$ 600 keV (detected by CdTe cells) and 150^o x 40^o for electrons in the range of 80 to $\sim$ 600 keV (detected by Si cells only). The direction of the detected electrons (hence their pitch-angle) can be estimated from coincidence between the Si cells and CdTe cell rows. This will provide an important complementary information to the measurements of XGRE.

The effective area versus energy of IDEE for detecting electrons was estimated with the GEANT4 mass model of the full TARANIS spacecraft, using the same methodology as for XGRE. An electron is detected if it deposits at least 80 keV on a Si cell or at least 350 keV on a CdTe cell. The effective area is presented in Figure 2.b. (~~black~~ blue curve). It shows a threshold E_I^t of about 610 keV below which the effective area is essentially due to the Si cells, and therefore very small (less than 1 cm^2). ~~E_I^t~~ As seen in Figure 1.d., the Si cells are mounted behind a $\sim$ 4 mm thick collimator with a narrow slit, allowing only a small fraction of the low energy electrons to go through the entrance window and reach the Si cells. Notice that two 0.2 mm thick aluminium fins are also present.

The value of $E_I^t = 610$ keV is the sum of ~~the~~ 350 keV (detection threshold) plus $\approx$ 260 keV, that is the average energy deposited on the 0.65 mm thick aluminium ~~layer~~ sheet covering the CdTe cells (see figure 1.d.). The effective area increases to about 28 cm^2 at 1.5 MeV, where all the electrons can cross the aluminium cover, and then goes up to about 20 cm^2 at 4 MeV and $\approx$ 38 cm^2 at 10 MeV, mostly due to the scattering of the particles to larger distance, and remains constant for higher energies.

The effective area averaged over a TEB spectrum, σ_I^{TEB}, can be calculated to be about 22 cm^2 (see Appendix A for the method used). If IDEE or XGRE ~~detects~~ triggers on a TGF or a TEB event, they will be able to trigger the other instrument : we should then consider the TARANIS spacecraft as a detector of TEB with an averaged effective area σ_T^{TEB} of about 255 cm^2.

3 Comparison between instruments

In this section we present a comparison of the performances of XGRE and IDEE with those of RHESSI, Fermi-GBM and AGILE-MCAL, in the context of TGFs, without including CGRO-BATSE in the comparison. CGRO-BATSE detected 79 TGFs between the years 1991 and 2000, some of them being clearly identified as TEBs (Dwyer et al., 2008). But we did not include it because this number of TGF is significantly smaller than for RHESSI, Fermi-GBM and AGILE. Furthermore, BATSE only triggered on long events (it had a trigger window that could not be lower than 64 ms), over-estimated their durations and under-estimated their brightnesses (Grefenstette et al., 2008; Gjesteland et al., 2010); thus making it a lot harder to separate between ~~TGFs events and TEBs~~ TGF and TEB events, compared to the other instruments.

3.1 TGF detection performance

The Reuven Ramaty High Energy Solar Spectroscopic Imager (RHESSI) is a NASA spacecraft designed for the study of high energy radiation from the sun. It uses an array of nine high purity germanium detectors cooled down to liquid nitrogen temperature. A detailed description of the detector is presented in Lin et al. (2002); Smith et al. (2002). A response matrix of the RHESSI detector in the TGF context is publicly available ~~from~~ (see Section 7 on data availability). The provided matrix is already averaged for the spacecraft position and attitude. From this matrix, we can deduce the effective area versus energy of the detector, that is presented in Figure 2.a. As indicated in Ostgaard et al. (2012), RHESSI has an effective area for detecting TGF σ_R^{TGF} of about 256 cm^2

The Astro-Rivelatore Gamma a Immagini Leggero (AGILE) is a satellite from the Italian Space Agency dedicated to the study of high energy gamma-ray (typically above 50 MeV) in the universe. The mini-calorimeter (MCAL) detector uses 30 cesium iodide (CsI) scintillator bars and can be used to detect lower energy gamma-rays (above 400 keV). It is presented into details in Tavani et al. (2009); Labanti et al. (2009). The effective area versus energy for AGILE-MCAL is taken from Marisaldi et al. (2015) and reproduced in Figure 2.a. As indicated in the same article, AGILE-MCAL has an effective area for detecting TGF ~~$\sigma_A^{TGF} = 220$ of about~~ σ_A^{TGF} of 220 cm^2.

The Gamma-Ray Burst Monitor (GBM) on-board the Fermi spacecraft is presented into details in Meegan et al. (2009). GBM is made of 12 sodium iodide (NaI) cylindrical detectors, sensitive in 20 keV - 10 MeV energy range, and 2 bismuth germanate (BGO) cylindrical detectors sensitive from 200 keV to 40 MeV. Regarding the NaI detectors, the photons above 1 MeV are counted in a single channel and not used for spectroscopy, but they are included for the TGF counts and the search algorithm. The effective area for high energy photons can be calculated from an average of response matrices generated by the *gbmrspgen* tool, developed by the Fermi-GBM collaboration (see Section 7 Data availability) The response matrix of GBM for a given event depends on the position and attitude of the spacecraft. To get an average effective area of the GBM detectors, we calculated an average matrix from 94 matrices that where generated from the 94 GBM triggered TGF of 2013. The effective area versus energy of the BGO and NaI detectors are presented in Figure 2.a.

As presented in Briggs et al. (2013), the effective area that should be used to detect TGF is 160 cm^2 for each BGO detector. Our calculation from the response matrices show that it should be about 33 cm^2 for each NaI detector, giving a total σ_F^{TGF} of about 716 cm^2 for Fermi-GBM. A summary of these averaged effective area for detecting TGF is presented in Table 1.

Below 30 keV, the NaI detectors of Fermi-GBM have the best effective area that ranges between 40 cm^2 and 300 cm^2. However, from simulation results it is not expected that TGF detected at satellite altitude show a lot of photons at these energies (Sarria et al., 2015), though this part of the spectrum has not been properly detected yet. Between 30 keV and 220 keV, XGRE has the best effective area (350-850 cm^2), that is about 1.4 higher than Fermi-NaI detectors, and 5 times higher than RHESSI. For higher energies, it falls and goes below AGILE-MCAL and Fermi-BGOs at about 1 MeV ($\sim$280 cm^2) and below RHESSI at about 2 MeV ($\sim$250 cm^2). From around 760 keV, the effective area of AGILE-MCAL increases greatly, and reaches about 750 cm^2 at 20 MeV, making it about twice better than RHESSI and Fermi-BGOs and three times better than XGRE. The uncertainties on the effective area values presented in this section are discussed in Appendix B.

RHESSI, Fermi and AGILE suffered from issues related to the fact that their design is not perfectly suited to detect very bright and short events such as TGFs. Concerning AGILE, this issue was likely solved after the disactivation of its anti-coincidence shield (Marisaldi et al., 2015). Depending of the processing algorithms and the electronics used by the detector, this can cause several issues, such as under-estimating the number of counts for bright TGFs (because of the detector's "dead time"), over-estimating the duration of bright TGFs, or incorrectly measuring photon energies (because of pulse "pile-up").

For Fermi GBM detectors, the nominal dead time lasts 2.6 μs, but it goes up to 10.4 μs if the overflow channel is filled, i.e. there is a count with energy above 1 MeV on a NaI detector or a count with energy > 40 MeV on a BGO detector. NaI detectors have a high rate of overflow counts, making TGF spectra obtained from them very hard to analyse in practice. On the other hand, these problems are less important on the BGO detectors, allowing correction and study of spectra from single TGF events (Mailyan et al., 2016).

XGRE uses Lanthanum Bromide crystal scintillators coupled with fast electronics, resulting in a dead time of 350 ns and a pile up time of 150 ns, giving a capability to count up to ~ 9 photons/μs (each of the three sensors being independent), that should be enough to avoid dead time or pile-up issues up to a count rate of about 10 million counts per second. Thus XGRE should derive precise measurements of light-curves and spectra, even for the shortest TGF.

The dead time of IDEE is less than 4 μs. It should not suffer of important dead times issues when detecting TEBs, since they show about 20 times less particles/cm^2/ms at satellite's altitude compared to TGFs (see Figure 3), and IDEE also has a relatively small effective area.

The TGF detection methods used by RHESSI, Fermi-GBM and AGILE-MCAL are described respectively in Gjesteland et al. (2012); Bri
Concerning XGRE, a TGF event can trigger if a given number of counts is reached within a 10 μs window. This number can be changed between half-orbits, and will be comprehensively tested during the spacecraft commissioning phase. There is also another trigger window working the same way but with a duration of 100 μs. It is made for (short) Gamma-Ray Bursts detection, but it is not excluded it could trigger on some TGF or TEB events. Detected particle prior to the trigger timer are saved (with an adjustable number). All the particles detected after the trigger time are saved until the TGF ends.

The IDEE instrument uses a dynamical algorithm which evaluates a floating background (in preselected energy range and Si/CdTe cell type) over selected time periods, based on Poisson distribution assumption and using a dynamic threshold. The IDEE instrument will trigger on TEB events, that will also trigger all the instruments of the TARANIS payload (including XGRE).

3.2 TEB detection performance

RHESSI, Fermi-GBM and AGILE-MCAL were not designed to detect electrons or positrons, therefore no response matrix is provided for these particles. Nevertheless, we could proceed to Monte-Carlo simulations of these detectors to get a basic idea of their performances for detecting TEBs.

The RHESSI detectors are surrounded by several millimeters of aluminum (Dwyer et al., 2012), that only very high energy electrons can cross.

Using a complete mass model of the RHESSI spacecraft (D. Smith, private communication, 2016), we could estimate its effective area for different electron incident energies. The procedure we followed is different that from XGRE/IDEE, since the orientation (attitude) of the spacecraft is not known and has no reason to point towards Earth like for TARANIS. Therefore we simply draw the particles randomly and uniformly over all directions around the spacecraft.

The effective area of RHESSI against electrons is displayed in Figure 2.b. It is < 1 cm^2 below 400 keV and then it rises to about 4 cm^2 at 1 MeV and then increases with energy until it reaches about 500 cm^2 at 20 MeV, due to important bresmstrahlung emissions. Using the same method as for XGRE, we could estimate an effective area σ_R^{TEB} of RHESSI averaged for a typical TEB event of about 74 cm^2.

Regarding Fermi-GBM, GEANT4 detailed models of single BGO and NaI detectors are available as GDML files as part of the GRESS software (Kippen et al., 2007). A NaI detector is covered by an aluminium parts (including the ~~PMT~~photo-multiplier tube), and one side of the crystal has a 0.2 mm thick berylium window and a 0.7 mm thick silicone layer in-between the two. The BGO detector has some dense parts on both side (including the photo-multiplier tubes) and the rest is covered with a ~ 3 mm thick carbon fiber (CRFP), and maintained by two titanium rings.

These single detector models are not enough to estimate the reponse of Fermi-GBM to electrons, because they do not take into account their accommodation on the spacecraft, nor the entire spacecraft (e.g. platform, subsystems, and LAT detector). We could not have access of to the full mass model of the Fermi satellite, but we could build a very simplified version, by looking to several Fermi-GBM documents; in particular (Meegan et al., 2009) and the references therein. Our simplified model contains the biggest parts of the spacecraft with approximative densities, and the 2 BGO and 12 NaI detectors are accurately placed. We think this model is reasonable for electrons since they get easily absorbed by the elements of the spacecraft, and also we only need a basic estimation of the GBM response to electrons.

The response of GBM to mono-energetic electron beams is presented in Figure 2 b. We followed the same procedure as for RHESSI (the particles are drawn randomly and uniformly over all directions around the spacecraft). The effective areas show threshold energies ($E^t_{NaI} \approx 500$ keV, $E^t_{BGO} \approx 1.5$ MeV) below which the effective area is very small. Below these energies, the electrons or positrons can hardly reach the crystals, because they are absorbed by surrounding materials. Above these threshold energies, the leptons have enough energy to have a chance to reach the crystals, and the effective area increases with increasing kinetic energy. This increase is because electrons with higher energy will scatter to higher distances in the spacecraft and will also produce more bremsstrahlung photons and with higher energies. For 20 MeV electrons, it reaches a value of about 770 cm^2 for the sum of the 12 NaI and 325 cm^2 for the sum of the two BGO. The response to positron is similar to the response to electrons, with the addition of a constant value, that is about 690 cm^2 in this case. As for other instruments, we can use the method presented in Appendix A to calculate a TEB-averaged effective area for Fermi-GBM, that is $\sigma_F^{TEB} \approx 350\,\mathrm{cm}^2$

Regarding AGILE, the full mass model was provided by the AGILE team (M. Marisaldi, private communication, 2016). The MCAL detector on the AGILE spacecraft is surrounded by several elements (e.g. the MITA spacecraft Bus, the GRID, the Super-AGILE, the anticoincidence system or the carbon fiber structure surrounding the CsI bars) that will absorb a significant amount of energy of the electrons before they can reach the CsI crystals (Longo et al., 2002; Cocco et al., 2002; Labanti et al., 2009). We could perform simulation to check the response of MCAL to electron and positron beams, following the

same procedure as for RHESSI and Fermi-GBM. The results are displayed in Figure 2.b and 2.c. (red curves). All the incident electrons with kinetic energies below about 3 MeV are absorbed before reaching the CsI bars. Above this energy, the effective area increases with increasing energy, mainly due to the production of bremsstrahlung photons that can reach the detectors. It reaches ~ 430 cm^2 at 20 MeV, where a lot of bremsstrahlung photons are produced. As for the other instruments, the response to positron is similar to the response to electrons, with the addition of a constant value (about 100 cm^2 in this case) due to photons produced by positron annihilation with the spacecraft. It results in an effective area σ_A^{TEB} averaged on a TEB spectrum of about 25 cm^2 for AGILE-MCAL. All the TGF and TEB effective areas are summarized in Table 1. The uncertainties on the effective area values presented in this section are discussed in Appendix B.

~~Concerning~~ For all these detectors, "dead times" ~~or~~ and "pile-up" ~~issues, all these detectors did not have any important problem concerning TEB~~ effects are not a big issue concerning TEB detection. Indeed, the flux (particles/cm^2/ms) for a TEB event at satellite altitude is usually about 20 time less than for TGF (see Figure 3), and their averaged effective area are also several times smaller for electrons than for gamma-rays.

4 Estimating TGF/TEB detection rates

4.1 Past TGF and TEB detections

The AGILE TGFs of the second catalog are given between 03/23/2015 and 06/23/2015, and contains 279 TGFs (Marisaldi et al., 2015). Taking into account that TGF are slightly more likely to be detected during this time period than the average of the rest of the year, it corresponds to about $N_A = 1070$ TGFs/year. For RHESSI, the detection rate is about $N_R = 350$ TGF/year for the second catalog (Ostgaard et al., 2015). For Fermi, by looking to publicly available catalog (http://fermi.gsfc.nasa.gov/ssc/data/access/gbm/tgf/), we could estimate that about $N_F = 650$ TGFs/year were detected after the offline searching method was set up (Briggs et al., 2013). All these values are summarized in Table 2.

Concerning Terrestrial Electrons Beams (TEBs), they were detected by RHESSI and Fermi. RHESSI detected clearly only two TEB events, and one of them was presented (Smith et al., 2006). This number is too low to permit an estimation of the number of TEB event that will be detected by TARANIS. As discussed in the previous section, Fermi-GBM has a much better sensitivity to electrons than RHESSI, and could detect about 24 events between August 2008 and February 2015, giving 3.7 TEBs/year.

No TEB event was reported by AGILE, and we speculate this is because the effective area for detecting TEB is not high enough (≈ 25 cm^2), and is actually mostly due to bremsstrahlung or annihilation photons produced by the electrons/positrons (see previous section).

4.2 Simulated Flux Profiles

Using the MC-PEPTITA Monte-Carlo model (Sarria et al., 2015), we estimated average flux profiles of gamma-rays and electrons detected by the satellites and associated to TGFs. The source is assumed to follow an energy spectrum $\propto 1/E \times$

$exp(-E/(7.3\mathrm{MeV}))$. The production altitude is uniformly sampled between 12 and 15 km and it is located at ($\theta = -13^o, \phi = 32^o$) geodetic coordinates. The opening angle is uniformly sampled between 0^o and 40^o. The source is also tilted by an angle ψ that is uniformly sampled between 0 and 10^o.

Concerning the time distribution of the source, there are currently two different results. On one hand, by comparing simulated TGFs with AGILE data, Marisaldi et al. (2015) suggests that, at the source, the TGF is created almost instantaneously, so that the TGF durations are mainly due to delays due to scatterings in the atmosphere, and long duration TGFs may be a succession of multiple pulses. On the other hand, by comparing simulated TGFs with Fermi data, Fitzpatrick et al. (2014) concluded that the source distribution is not created instantaneously for a vast majority of Fermi-GBM TGFs and indicated that a good fit to the Fermi data is a time distribution of the TGF source following a Gaussian (Normal) distribution with $\sigma = 50\,\mu$s. The results of MC-PEPTITA simulations suggest a source duration in-between an almost instantaneous source and a normal source duration of $\sigma = 50\,\mu$s . Assuming a normal distribution definition $\propto \exp\left(-t^2/\left(2\sigma^2\right)\right)$ for the TGF photons when they are produced, and using a standard deviation of $\sigma = 20\,\mu$s, results to t_{90} durations of TGFs down to $\sim 60-70\ \mu$s; that corresponds to the lowest durations observed by the Fermi spacecraft (Fitzpatrick et al., 2014).

From Fermi data, Fitzpatrick et al. (2014) indicates that Fermi typically detects about 0.08 photons/cm^2 over a TGF duration of 200 μs (giving 0.4 photons/cm^2/ms) at a radial distance of 500 km between the satellite position and the position of the source of the TGF. We used this value to give a scale to the flux distributions presented in Figure 3, that is obtained by assuming that 4.4×10^{17} photons (with energies > 20 keV) are produced at the source.

The flux profiles resulting from the simulations are presented in Figure 3.a. The fluxes are presented as a function of the radial distance (r_d) between the source position of the TGF (projected at the altitude of the satellite) and the satellite. The three presented altitudes approximately correspond to AGILE (490 km), Fermi (550 km) and TARANIS (700 km). The fluxes are expressed in terms of particles/cm^2/ms, considering photons and electrons. Figure 3.b. presents the corresponding time durations (t_{90}).

Below r_d =100 km, the photon flux at an altitude of 490 km is about 31 % higher than the flux at 560 km, and twice the flux at 700 km. This difference of fluxes corresponds to the $1/R^2$ variation expected from an isotropic point source detected from various distances. At about r_d =300 km, the photon fluxes are similar for the three altitudes. Above $r_d \approx 600$ km, the flux at 700 km is about 57% higher than the flux at 560 km, and the flux at 560 km is 39% times higher than at 490 km altitude.

Concerning electrons, the fluxes are close at the three considered altitudes, so we only represented the flux at 550 km. It is important to note that the time scattering of electrons detected at satellite altitude can vary significantly depending on the length of the magnetic field line the particles have to travel, that depends on the coordinates of the spacecraft (higher absolute latitudes usually meaning longer field lines). This time dispersion is because electrons are produced with various pitch angles and energies, that will imply various propagation speeds along the geomagnetic field lines (Dwyer et al., 2008; Sarria et al., 2016). The results shown here are for a given magnetic field line of about 6000 km length, that can be roughly considered as an average TEB case. In Figure 3, the flux of electrons is about 3 times higher if detected in the hemisphere where the the TGF is produced. The spatial fluxes (electrons/cm^2) are actually quite close on both hemispheres, but, as showed in Figure 3.b., the t_{90} time durations of the TEBs are about 3 times higher in the opposite hemisphere.

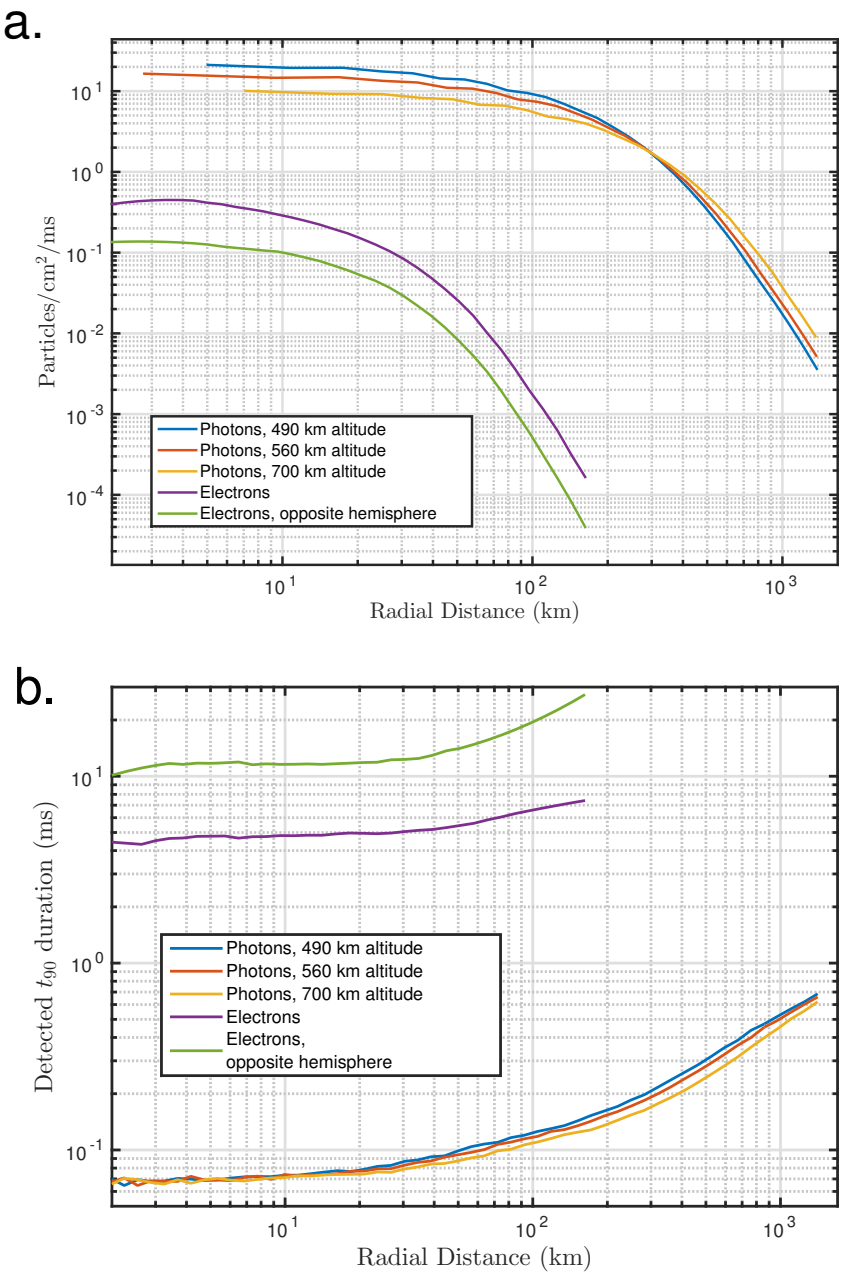

Figure 3. Results of MC-PEPTITA simulations. **a.** Flux profile versus radial distance between the TGF source (projection at satellite altitude) and the satellite; for photons (various altitudes) and electrons (seen at the hemisphere of production and in the opposed hemisphere). The two electron profiles correspond to a detection altitude of 560 km, but are very close for 490 or 700 km altitude. **b.** t_{90} durations associated to the flux profiles. Like for the flux profiles, the electron distributions stay very similar at 490 or 700 km altitude.

4.3 Estimating a map of TGFs that can be detected by satellites.

~~We propose to build an~~ An approximative map of TGFs that can be detected by satellites was built, based on the TRMM-LISS and OTD global lightning density map (Cecil et al., 2014). Compared to this distribution, it was noticed that the TGF density detected by satellites tends to be higher towards the equator. Actually, this is supposed to be due to the fact that the tropopause is higher for latitudes closer to zero, where TGF photons have to cross less atmosphere before reaching space, and can be more easily detected by satellites. Let $\rho_L(\theta,\phi)$ be the lightning density from the LISS/OTD database for a given latitude and longitude. Let $T(\theta)$ be an approximative profile of the tropopause height as function of latitude. We used data obtained from Lewis (2009) that was fit by a simple Normal distribution $T(\theta) \propto \exp\left[((\theta-\theta_0)/2\sigma_\theta)^2\right]$ with parameters $\theta_0 = 0.8746^o$ and $\sigma_\theta = 37.49^o$. Then the TGF density at a given latitude and longitude is assumed to follow :

$$\rho_{TGF}(\theta,\phi) \propto \rho_L(\theta,\phi) \times [T(\theta)]^\beta \quad (1)$$

The proportionality sign ($\propto$) denotes the fact that we do not define an absolute scale for this density, and therefore all the estimations given afterwards will only use ratios of summed values of $\rho_{TGF}(\theta,\phi)$. Equation (1) shows that the tropopause profile is set at a power β that we are using as a free parameter, ~~that~~ and will be adjusted to get the best possible agreement between this simple model and the observations. This estimated TGF global production map is displayed in Figure 4. This Figure also shows the groundtracks of RHESSI, Fermi, AGILE and TARANIS (planned). They have been calculated using the Two-Line Element from the CELESTRACK database (https://www.celestrak.com/NORAD/elements/). The orbit of TARANIS is assumed to be similar to that of the DEMETER satellite. RHESSI, Fermi and AGILE show equatorial orbits with various inclinations (38^o, 25.6^o and 2.5^o respectively), whereas TARANIS will follow a quasi-polar sun-synchronous orbit. This orbit is not the best for detecting TGFs since it will have a significantly reduced coverage of the equatorial region where TGF are more likely to be detected, and the impacts on TGF detection rates are discussed in the next section. However, the orbit of TARANIS covers almost uniformly all latitudes and should permit to determine a global distribution of TGF without orbital bias.

4.4 Estimating TGF and TEB Detection Rates

Each detector ~~will have~~ has a minimal threshold of counts n_X^{min} for any detected event to be significantly above the background level to be considered as a ~~"detected TGF"~~TGF. Gjesteland et al. (2012) indicates that $n_R^{min} = 11$ (for the RHESSI second catalog) and Ostgaard et al. (2012) indicates $n_F^{min} = 19$ for Fermi-GBM. The value for AGILE ($n_A^{min} = 10$) is found by the TGF that has the lowest number of count in the AGILE second catalog (Marisaldi et al., 2015). The value of n_G^{min} for TARANIS-XGRE is assumed to be also 10 but is hard to predict and will depend on the in-flight background. We should wait for the instrument to be launched to be able to know precisely which value will be used. Appendix B discuss how variations on n_T^{min} affects the results presented in this section.

The ratio between this threshold value n_X^{min} and the averaged effective area σ_X^{TGF} gives a limit of sensitivity for the instrument. Combining this limit with the radial distance flux profiles (section 4.2 and Figure 3), we can deduce a limit distance

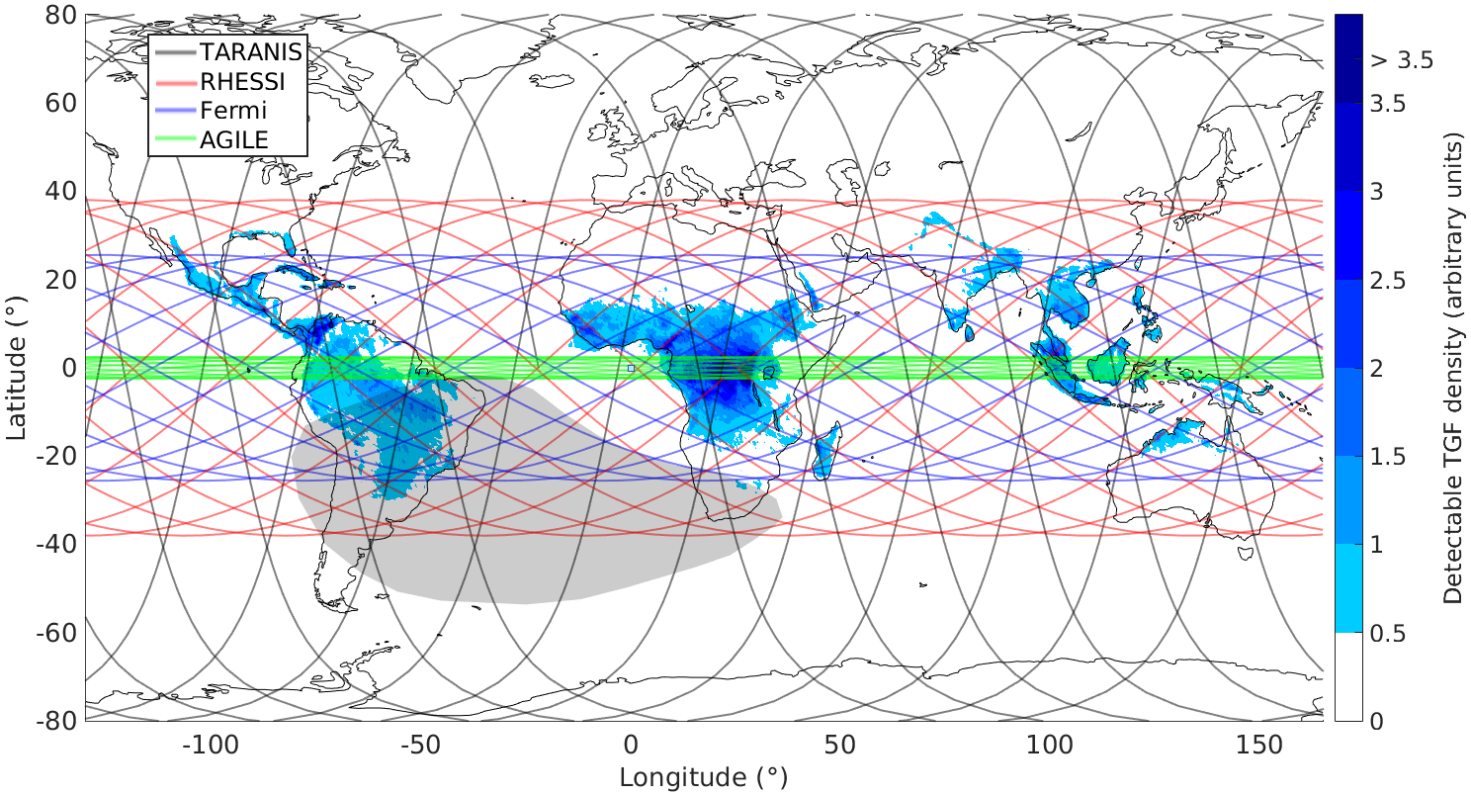

Figure 4. Estimated global detectable TGF density map, and groundtracks of the orbits of TARANIS (planned), RHESSI, Fermi, and AGILE. The ~~dark~~ grey area denotes an approximative South-Atlantic Anomaly assumed for the simulations, and where TGF can occur but no detection by satellites is possible due to high background.

R_X^{lim} corresponding to this sensitivity. The limit of sensitivity of Fermi is ≈ 0.053 photons/cm^2/ms (= 19 photons / 716 cm^2 / 500 μs) and corresponds to a limit radius of $R_F^{lim} \approx 795$ km. This value is consistent with the maximum distance between the TGF source positions and Fermi footprints given using WWLLN associations (Briggs et al., 2013; Fitzpatrick et al., 2014). We can also determine $R_R^{lim} = 694$ km that is reasonably close to the largest distance found between RHESSI's position and the WWLLN match of the TGF source location (Nisi et al., 2014). Using the simulated photon flux and time profiles at 490 km altitude, we could estimate $R_{XG}^{lim} = 648$ km for AGILE-MCAL. Using the simulated photon flux and time profiles at 700 km altitude, we could estimate ~~$R_{XG}^{lim} = 917$~~ $R_{XG}^{lim} = 820$ km for TARANIS-XGRE (corresponding to a t_{90} duration of about 420 μs). All theses values are summarized in Table 2.

Knowing R_X^{lim}, the orbit of the satellite, and the detectable TGF density map, we can deduce a detection efficiency, expressed as $E_{X/A}$. Since we did not find an absolute scale for it, we only expressed it relatively to AGILE (second catalog), which has the highest TGF detection rate.

This detection efficiency is computed using the following algorithm :

- We consider a step of time δ_t =120 seconds, that is small enough compared to the scale of duration of one orbit of about 5400 seconds.
- At each time step corresponds a position of the satellite (θ_i^X, ϕ_i^X).
- at each position, the TGF densities from the map ($\rho_{TGF}(\theta, \phi)$) are summed within a radius of R_{lim}^X around (θ_i^X, ϕ_i^X), giving a quantity Σ^X.
- Σ^X is incremented this way over 48 hours (1442 steps).
- if (θ_i, ϕ_i) is inside the South-Atlantic Anomaly (SAA), Σ^X is not incremented. We use the approximative SAA area presented ~~in dark~~ as a grey area in Figure 4.

The ratio Σ^X/Σ^A (between a given satellite X and AGILE) gives a detection efficiency $E_{X/A}$, whose values are summarized in Table 2. Applying these efficiencies to the AGILE detection rate gives detection rate estimates of 649.2 TGFs/year for Fermi and 349.7 TGFs/year for RHESSI. For both, the relative difference with the observed detection rates are less than 1%. Note that the value of the parameter β for the detectable TGF map (see section 4.3) was adjusted to $\beta = 7.1$ in order to minimize these differences.

One last parameter to be taken into account is the diurnal cycle of lightning. Lightning activity was found to be non-uniform with local time and has maximum around 17h and minimum around 11h (Cecil et al., 2014). TARANIS, with its sun-synchronous orbit will always be at a local time between 22h30-2h and 10h30-14h. The other satellites have equatorial orbits therefore their local time is almost uniformly distributed between 0h and 24h. It implies that XGRE will miss an extra 24% of TGF compared to the other satellites. Finally, our estimation gives about ~~225~~ 200 TGFs/years for TARANIS. All the important parameters used for this estimation are summarized in Table 2.

	h_X (km)	n_X^{min} (counts)	R_X^{lim} (km)	$E_{X/A}$	$N_X^{TGF,obs}$ (TGFs/year)	$N_X^{TGF,est}$ (TGFs/year)
RHESSI (Second catalog)	565	11	694	32.7 %	350	349.7
Fermi-GBM	543	19	795	60.7 %	650	649.2
AGILE-MCAL (Second catalog)	491	10	648	100 %	1070	1070
TARANIS-XGRE	700	10 ?	~~917~~ 820	~~27.64~~ 24.9 %	?	~~225~~202[a]

[a] Takes into account the diurnal correction.

Table 2. Altitudes, detection count thresholds, limit radii, detection efficiencies and number of TGFs per year (observed and estimated) for the considered satellites.

The catalog of Fermi GBM TEBs presents 24 events between 08/07/2008 and 02/02/2015, giving $N_F = 3.7$ TEBs/year. These events present a minimum count of $n_F^{min} \approx 150$ for the event ID TEB130521580. Since XGRE will discriminate electrons from photons, this threshold should be similar to TGF, i.e. $n_{XGRE}^{min} = 10$. As in the case of TGFs, this value is hard

to estimate and the correct value will only be known after in-flight tests of the instrument. As discussed in section 4.2, the effective area of TARANIS (XGRE+IDEE) for detecting TEB could be estimated : ~~$\sigma_G^{TEB} = 255, \mathrm{cm}^2$~~ $\sigma_G^{TEB} = 255\,\mathrm{cm}^2$. This TEB average effective area could be estimated for Fermi-GBM, giving $\sigma_R^{TEB} \approx 350\,\mathrm{cm}^2$.

To determine the TEB detection efficiency, the algorithm presented for the TGF case has to be modified. If the satellite is located at given coordinates, the considered density is not the density at this point, but the sum of the two densities located at the two magnetic footprints of the field line. These coordinates are determined from MC-PEPTITA runs that can track the electrons in the geomagnetic field. In these simulations, the electrons are drawn at 100 km altitude with various pitch angles (this altitude being approximately the altitude where the secondary electrons from TGF can escape Earth's atmosphere).

From all this information, we can calculate detection efficiencies : between TARANIS and Fermi $E_{T/F}^{TEB} = 885\,\%$. As for the TGF estimation, we also have to account for the diurnal ~~effect~~ correction for the TARANIS case, and our final estimate is about 25 TEBs/year. All the important parameters used for this estimation are summarized in Table 3.

	n_X^{min} (counts)	R_X^{lim} (km)	$E_{X/F}$	$N_X^{TEB,obs}$ (TEBs/year)	$N_X^{TEB,est}$ (TEBs/year)
Fermi-GBM	~ 150	23	100 %	3.7	3.7
TARANIS (XGRE+IDEE)	10 ?	72	885 %	?	25[a]

[a] Takes into account the diurnal correction.

Table 3. Count thresholds, limit radii, detection efficiencies and number of TEBs per year (observed and estimated) for the considered satellites.

5 Conclusions

The TARANIS spacecraft will have two important instruments to study TGFs and TEBs : XGRE and IDEE. XGRE will detect both electrons and X/gamma-rays, with the ability to discriminate one type of particle from the other. The IDEE instrument is focused on electrons, with the ability to estimate their pitch angle. Both instrument will be able to trigger one another.

Using Monte-Carlo simulations, mass models and a standard TGF spectrum, we could estimate that XGRE will have about 425 cm^2 effective area for detecting TGFs. The combination of XGRE and IDEE will give about 255 cm^2 effective area for detecting electrons associated to TGFs. With a count rate capability of about 10 million counts/second, XGRE should suffer of much less "dead time" issues during bright TGF events, that were detrimental for previous detectors. Thus XGRE should derive precise measurements of light-curves and spectra, even for the shortest TGF.

Using Monte-Carlo simulations of the TARANIS, RHESSI AGILE, and Fermi spacecrafts, we could estimate the response of their detectors to electrons and positrons, and provide a quantitative comparison between them. By combining this knowledge with an approximative world map of detectable TGF density and with MC-PEPTITA Monte-Carlo simulations of TGF propagation in the atmosphere, we could build an accurate model of the TGF detection rates of RHESSI, AGILE, and Fermi. It could be used to estimate that TARANIS should detect about ~~225~~ 200 TGFs/year and 25 TEBs/year.

6 Code availability

The GEANT4 mass model of TARANIS satellite with XGRE and IDEE instrument is still under developpement and is not publicly available~~yet~~. But simulations in specific configurations can be requested to the corresponding author, contact David Sarria (dsarria@apc.in2p3.fr).

The GEANT3 mass model of the RHESSI detector and spacecraft can be requested to David Smith (dsmith@scipp.ucsc.edu)

The GEANT3 mass model of the AGILE detectors and spacecraft can be requested to Martino Marsaldi (Martino.Marisaldi@uib.no), Marcello Galli (marcello.galli@enea.it) and Francesco Longo (franzlongo1969@gmail.com).

The GEANT4 GDML mass model of the Fermi-GBM BGO and NaI detection units are publicly available as part of the GRESS software (Kippen et al., 2007) . For this work, an approximative Fermi spacecraft model was built, that roughly respects the mass distribution of the spacecraft known from literature (see Meegan et al. (2009) and references therein).

MC-PEPTITA simulations can be requested ~~, contact~~ to David Sarria (dsarria@apc.in2p3.fr). MC-PEPTITA program was developed under a contract of Centre National d'Etudes Spatiales (CNES) and Direction Generale de l'Armement (DGA), whose permissions are required in order to get access to the source code.

7 Data availability

The data generated for this work can be requested to the corresponding author, contact David Sarria (dsarria@apc.in2p3.fr).

The response matrices of Fermi GBM detectors are publicly available using the *gbmrspgen* tool, whose usage is documented in the following website https://fermi.gsfc.nasa.gov/ssc/data/analysis/scitools/gbmrspgen.html . The response matrix of the RHESSI instrument in the TGF context was publicly made available by D. M. Smith in the following website http://scipp.ucsc.edu/~dsmith/tgflib/public/. The effective area versus energy against X/gamma photons (in the TGF context) for AGILE-MCAL is taken from Marisaldi et al. (2015) .

The $V2.3.2014$ gridded satellite lightning data were produced by the NASA LIS/OTD Science Team (Principal Investigator, Dr. Hugh J. Christian, NASA / Marshall Space Flight Center) and are available from the Global Hydrology Resource Center (http://ghrc.msfc.nasa.gov).

~~The response matrices of Fermi GBM detectors are publicly available using the *gbmrspgen* tool, whose utilisation is detailed in the following website~~

~~The response matrix of the RHESSI detector is publicly available in the following website .~~

Appendix A: Determining detectors' averaged effective areas

We use a custom method to determine the average effective area of an instrument for detecting TGFs (or TEBs). Using a simulation of a given instrument, we can launch mono-energetic beams of particles of energy E and determine the number that has been detected $N_d(E)$. We can then determine $S_X^Y(E)$, the effective area at the energy E, where Y corresponds to the event

type (TGF or TEB) and X designates the detector (XGRE, IDEE, RHESSI, GBM or MCAL). Assuming there are N_{launch} particles drawn uniformly from an area S_{launch} (that should be higher than the area of the whole satellite) :

$$S_X^Y(E) = N_d(E) \times \frac{S_{launch}}{N_{launch}} \tag{A1}$$

$S_X^Y(E)$ can then be averaged over an assumed spectra of TGF (or TEB) to obtain a value σ_X^Y, characterizing the average effective area of the detector for detecting a TGF (or TEB) :

$$\sigma_X^Y = \frac{\int_{20\,kev}^{20\,MeV} f_Y(E)\, S_X(E)\, dE}{\int_{20\,kev}^{20\,MeV} f_Y(E)\, dE} \tag{A2}$$

Where $f_Y(E)$ is the assumed spectrum of the considered event type. We choose to use the photon and electron spectra at satellite altitude presented in the Figure 4 of Dwyer et al. (2008), assuming it is valid for all the orbits of previously mentioned experiments. We also assume that 10% of the electrons are actually positrons (as it is estimated from simulations of Terrestrial Electron Beams (Sarria et al., 2015)), and that the electron spectrum does not differ very much in its shape from the positron spectrum.

Appendix B: About uncertainties on the models used, and the impact of wrongly estimated effective areas and count thresholds of XGRE.

RHESSI, Fermi-GBM and AGILE-MCAL models have been done for X/Gamma-Ray detection, and such models are usually accurate at about 5%. Concerning electron/positron detection, the RHESSI, Fermi and AGILE models have not been done for this purpose and no calibration measurement were done against electrons (as far as we know), thus there is no easy way to know precisely what is the accuracy of their response to electrons/positrons and so to give an accuracy level for the effective areas presented in Figure 2 and in Table 1.

For TARANIS, using calibration measurement at detection unit level, the model was tested to be about 5% accurate against X/gamma-rays and (low energy) electrons. The real value of effective areas may vary from the values presented after the extensive analysis of the results of the calibration measurements on-board satellite (planned in 2018), and it is impossible to predict exactly how. When all the calibration measurements will be processed, the model should be accurate at less than 5 % for X/gamma-ray and electron detection. The response to positrons will be impossible to test against real measurements and will only rely on simulations.

Using the model presented in Section 4.4, it is possible to calculate what will be the sensitivity of a X percent inaccuracy of the estimated TARANIS effective areas on the final TGF and TEB detection rate estimation. The results are presented in Table 4.

A count threshold value of $n_T^{min} = 10$ (like in the main text) was assumed to get these estimations. Table 5 present how a change on n_T^{min} can impact our final TGF/TEB detection rate estimations (according to the model described in section 4.4).

TGF			TEB		
σ_T^{TGF} (nadir)	R_T^{lim}	$N_T^{TGF,est}$	σ_T^{TEB}	R_T^{lim}	$N_T^{TEB,est}$
425 cm²	820 km	202	255 cm²	72 km	25
382 cm² (10% error)	793 km	195	230 cm² (10% error)	70 km	23.6
340 cm² (20% error)	765 km	185	204 cm² (20% error)	68 km	22.3

Table 4. Effect of an over-estimated effective area $\left(\sigma_T^{XXX}\right)$ on the limit radius $\left(R_T^{lim}\right)$ and the TGF/TEB detection rate estimations $\left(N_T^{XXX,est}\right)$.

TGF			TEB		
n_T^{min}	R_T^{lim}	$N_T^{TGF,est}$	n_T^{min}	R_T^{lim}	$N_T^{TEB,est}$
10	820 km	202	10	72 km	25
12	775 km	189	12	68 km	22.3
15	724 km	170	15	64 km	19.7
20	663 km	149	20	59 km	17.6
30	582 km	130	30	51 km	13.2

Table 5. Effect of an under-estimated count threshold $\left(n_T^{min}\right)$ on the limit radius $\left(R_T^{lim}\right)$ and the TGF/TEB detection rate estimations $\left(N_T^{XXX,est}\right)$.

Author contributions. David Sarria prepared most of the manuscript. David Sarria, Remi Chipaux, Jean-Pierre Baronick contributed to the GEANT4 model of the XGRE instruments and TARANIS satellite. David Sarria performed all GEANT4 simulations (TARANIS XGRE, IDEE with satellite, and Fermi-GBM). Francois Lebrun, Pierre-Louis Blelly and Philippe Laurent provided a detailed review of the manuscript, and important feedback on the XGRE instrument, and instrument comparison. Remi Chipaux provided a review of the manuscript. Damien Pailot and Miles Lindsey-Clark provided important data to validate the GEANT4 model of the XGRE instrument, as well as important feedback on the instrument description (Section 2.1). Jean-Andre Sauvaud and Pierre Devoto provided the GEANT4 model of IDEE, important data to validate it. Jean-Andre Sauvaud, Pierre Devoto and Lubomir Prech contributed to the IDEE instrument part of the manuscript (Section 2.2). Lubomir Prech provided an important review of the IDEE instrument description. Philippe Laurent performed GEANT3 simulation on the RHESSI and AGILE mass models, that where provided by David Smith (RHESSI); Martino Marsaldi, Marcello Galli and Francesco Longo (AGILE).

Acknowledgements. We thanks D. Smith for providing the mass model the RHESSI Spacecraft, and discussion about its response to electrons. We thank M. Briggs for his help in estimating of the Fermi-GBM reponse to electrons. We thank M. Marisaldi, F. Longo and M. Galli for providing the mass model of the AGILE Spacecraft, and their help in discussing the response of MCAL to electrons.

This work was granted access to the HPC resources of CALMIP supercomputing center under the allocation 2015-p1505.

We thank the CNES (Centre National d'Etudes Spatiales) for its financial support.

The work of Lubomir Prech was supported by the Czech Science Foundation contract 17-06065S.

We would like to thank the two anonymous referees for their valuable comments and suggestions that helped to improve the quality of this work.

References

Agostinelli, S. et al.: GEANT4: A simulation toolkit, Nucl. Instrum. Meth., A506, 250–303, doi:10.1016/S0168-9002(03)01368-8, 2003.

Allison, J., Amako, K., Apostolakis, J., Araujo, H., et al.: Geant4 developments and applications, IEEE Transactions on Nuclear Science, 53, 270–278, doi:10.1109/TNS.2006.869826, 2006.

Briggs, M. S., Fishman, G. J., Connaughton, V., Bhat, P. N., Paciesas, W. S., Preece, R. D., Wilson-Hodge, C., Chaplin, V. L., Kippen, R. M., von Kienlin, A., Meegan, C. A., Bissaldi, E., Dwyer, J. R., Smith, D. M., Holzworth, R. H., Grove, J. E., and Chekhtman, A.: First results on terrestrial gamma ray flashes from the Fermi Gamma-ray Burst Monitor, Journal of Geophysical Research (Space Physics), 115, A07323, doi:10.1029/2009JA015242, 2010.

Briggs, M. S., Connaughton, V., Wilson-Hodge, C., Preece, R. D., Fishman, G. J., Kippen, R. M., Bhat, P. N., Paciesas, W. S., Chaplin, V. L., Meegan, C. A., von Kienlin, A., Greiner, J., Dwyer, J. R., and Smith, D. M.: Electron-positron beams from terrestrial lightning observed with Fermi GBM, grl, 38, L02808, doi:10.1029/2010GL046259, 2011.

Briggs, M. S., Xiong, S., Connaughton, V., Tierney, D., Fitzpatrick, G., Foley, S., Grove, J. E., Chekhtman, A., Gibby, M., Fishman, G. J., McBreen, S., Chaplin, V. L., Guiriec, S., Layden, E., Bhat, P. N., Hughes, M., Greiner, J., Kienlin, A., Kippen, R. M., Meegan, C. A., Paciesas, W. S., Preece, R. D., Wilson-Hodge, C., Holzworth, R. H., and Hutchins, M. L.: Terrestrial gamma-ray flashes in the Fermi era: Improved observations and analysis methods, Journal of Geophysical Research (Space Physics), 118, 3805–3830, doi:10.1002/jgra.50205, 2013.

Cecil, D. J., Buechler, D. E., and Blakeslee, R. J.: Gridded lightning climatology from TRMM-LIS and OTD: Dataset description, Atmospheric Research, 135-136, 404 – 414, doi:http://dx.doi.org/10.1016/j.atmosres.2012.06.028, http://www.sciencedirect.com/science/article/pii/S0169809512002323, 2014.

Cocco, V., Longo, F., and Tavani, M.: Simulation of the AGILE gamma-ray imaging detector performance: Part II, Nuclear Instruments and Methods in Physics Research A, 486, 623–638, doi:10.1016/S0168-9002(01)02160-X, 2002.

Cohen, M. B., Inan, U. S., Said, R. K., Briggs, M. S., Fishman, G. J., Connaughton, V., and Cummer, S. A.: A lightning discharge producing a beam of relativistic electrons into space, Geophysical Research Letters, 37, n/a–n/a, doi:10.1029/2010GL044481, http://dx.doi.org/10.1029/2010GL044481, 2010.

Dwyer, J. R., Grefenstette, B. W., and Smith, D. M.: High-energy electron beams launched into space by thunderstorms, Geophysical Research Letters, 35, n/a–n/a, doi:10.1029/2007GL032430, http://dx.doi.org/10.1029/2007GL032430, 2008.

Dwyer, J. R., Smith, D. M., and Cummer, S. A.: High-Energy Atmospheric Physics: Terrestrial Gamma-Ray Flashes and Related Phenomena, ssr, 173, 133–196, doi:10.1007/s11214-012-9894-0, 2012.

Fishman, G. J., Bhat, P. N., Mallozzi, R., Horack, J. M., Koshut, T., Kouveliotou, C., Pendleton, G. N., Meegan, C. A., Wilson, R. B., Paciesas, W. S., Goodman, S. J., and Christian, H. J.: Discovery of Intense Gamma-Ray Flashes of Atmospheric Origin, Science, 264, 1313–1316, doi:10.1126/science.264.5163.1313, 1994.

Fitzpatrick, G., Cramer, E., McBreen, S., Briggs, M. S., Foley, S., Tierney, D., Chaplin, V. L., Connaughton, V., Stanbro, M., Xiong, S., Dwyer, J., Fishman, G. J., Roberts, O. J., and von Kienlin, A.: Compton scattering in terrestrial gamma-ray flashes detected with the Fermi gamma-ray burst monitor, prd, 90, 043008, doi:10.1103/PhysRevD.90.043008, 2014.

Gjesteland, T., Østgaard, N., Connell, P. H., Stadsnes, J., and Fishman, G. J.: Effects of dead time losses on terrestrial gamma ray flash measurements with the Burst and Transient Source Experiment, Journal of Geophysical Research (Space Physics), 115, A00E21, doi:10.1029/2009JA014578, 2010.

Gjesteland, T., Østgaard, N., Collier, A. B., Carlson, B. E., Eyles, C., and Smith, D. M.: A new method reveals more TGFs in the RHESSI data, grl, 39, L05102, doi:10.1029/2012GL050899, 2012.

Grefenstette, B. W., Smith, D. M., Dwyer, J. R., and Fishman, G. J.: Time evolution of terrestrial gamma ray flashes, grl, 35, L06802, doi:10.1029/2007GL032922, 2008.

Inan, U. S., Piddyachiy, D., Peter, W. B., Sauvaud, J. A., and Parrot, M.: DEMETER satellite observations of lightning-induced electron precipitation, Geophysical Research Letters, 34, n/a–n/a, doi:10.1029/2006GL029238, http://dx.doi.org/10.1029/2006GL029238, 2007.

Kippen, R. M., Hoover, A. S., Wallace, M. S., Pendleton, G. N., Meegan, C. A., Fishman, G. J., Wilson-Hodge, C. A., Kouveliotou, C., Lichti, G. G., von Kienlin, A., Steinle, H., Diehl, R., Greiner, J., Preece, R. D., Connaughton, V., Briggs, M. S., Paciesas, W. S., and Bhat, P. N.: Instrument Response Modeling and Simulation for the GLAST Burst Monitor, in: The First GLAST Symposium, edited by Ritz, S., Michelson, P., and Meegan, C. A., vol. 921 of *American Institute of Physics Conference Series*, pp. 590–591, doi:10.1063/1.2757466, 2007.

Labanti, C., Marisaldi, M., Fuschino, F., Galli, M., Argan, A., Bulgarelli, A., Di Cocco, G., Gianotti, F., Tavani, M., and Trifoglio, M.: Design and construction of the Mini-Calorimeter of the AGILE satellite, Nuclear Instruments and Methods in Physics Research A, 598, 470–479, doi:10.1016/j.nima.2008.09.021, 2009.

Lefeuvre, F., Blanc, E., and Pinçon, J. L.: TARANIS-a Satellite Project Dedicated to the Physics of TLEs and TGFs, in: American Institute of Physics Conference Series, vol. 1118 of *American Institute of Physics Conference Series*, pp. 3–7, doi:10.1063/1.3137711, 2009.

Lewis, H. W.: A robust method for tropopause altitude identification using GPS radio occultation data, Geophysical Research Letters, 36, n/a–n/a, doi:10.1029/2009GL039231, http://dx.doi.org/10.1029/2009GL039231, 2009.

Lin, R. P., Dennis, B. R., Hurford, G. J., Smith, D. M., Zehnder, A., Harvey, P. R., Curtis, D. W., Pankow, D., Turin, P., Bester, M., Csillaghy, A., Lewis, M., Madden, N., van Beek, H. F., Appleby, M., Raudorf, T., McTiernan, J., Ramaty, R., Schmahl, E., Schwartz, R., Krucker, S., Abiad, R., Quinn, T., Berg, P., Hashii, M., Sterling, R., Jackson, R., Pratt, R., Campbell, R. D., Malone, D., Landis, D., Barrington-Leigh, C. P., Slassi-Sennou, S., Cork, C., Clark, D., Amato, D., Orwig, L., Boyle, R., Banks, I. S., Shirey, K., Tolbert, A. K., Zarro, D., Snow, F., Thomsen, K., Henneck, R., McHedlishvili, A., Ming, P., Fivian, M., Jordan, J., Wanner, R., Crubb, J., Preble, J., Matranga, M., Benz, A., Hudson, H., Canfield, R. C., Holman, G. D., Crannell, C., Kosugi, T., Emslie, A. G., Vilmer, N., Brown, J. C., Johns-Krull, C., Aschwanden, M., Metcalf, T., and Conway, A.: The Reuven Ramaty High-Energy Solar Spectroscopic Imager (RHESSI), solphys, 210, 3–32, doi:10.1023/A:1022428818870, 2002.

Longo, F., Cocco, V., and Tavani, M.: Simulation of the AGILE gamma-ray imaging detector performance: part I, Nuclear Instruments and Methods in Physics Research A, 486, 610–622, doi:10.1016/S0168-9002(01)02159-3, 2002.

Mailyan, B. G., Briggs, M. S., Cramer, E. S., Fitzpatrick, G., Roberts, O. J., Stanbro, M., Connaughton, V., McBreen, S., Bhat, P. N., and Dwyer, J. R.: The Spectroscopy of Individual Terrestrial Gamma-ray Flashes: Constraining the Source Properties, Journal of Geophysical Research: Space Physics, pp. n/a–n/a, doi:10.1002/2016JA022702, http://dx.doi.org/10.1002/2016JA022702, 2016JA022702, 2016.

Marisaldi, M., Fuschino, F., Tavani, M., Dietrich, S., Price, C., Galli, M., Pittori, C., Verrecchia, F., Mereghetti, S., Cattaneo, P. W., Colafrancesco, S., Argan, A., Labanti, C., Longo, F., Del Monte, E., Barbiellini, G., Giuliani, A., Bulgarelli, A., Campana, R., Chen, A., Gianotti, F., Giommi, P., Lazzarotto, F., Morselli, A., Rapisarda, M., Rappoldi, A., Trifoglio, M., Trois, A., and Vercellone, S.: Properties of terrestrial gamma ray flashes detected by AGILE MCAL below 30 MeV, Journal of Geophysical Research (Space Physics), 119, 1337–1355, doi:10.1002/2013JA019301, 2014.

Marisaldi, M., Argan, A., Ursi, A., Gjesteland, T., Fuschino, F., Labanti, C., Galli, M., Tavani, M., Pittori, C., Verrecchia, F., D'Amico, F., Østgaard, N., Mereghetti, S., Campana, R., Cattaneo, P., Bulgarelli, A., Colafrancesco, S., Dietrich, S., Longo, F., Gianotti, F., Giommi, P.,

Rappoldi, A., Trifoglio, M., and Trois, A.: Enhanced detection of terrestrial gamma-ray flashes by AGILE, Geophysical Research Letters, 42, 9481–9487, doi:10.1002/2015GL066100, http://dx.doi.org/10.1002/2015GL066100, 2015.

Marisaldi, M., Smith, D. M., Brandt, S., Briggs, M. S., Budtz-Jørgensen, C., Campana, R., Carlson, B. E., Celestin, S., Connaughton, V., Cummer, S. A., Dwyer, J. R., Fishman, G. J., Fullekrug, M., Fuschino, F., Gjesteland, T., Neubert, T., Østgaard, N., and Tavani, M.: High-energy radiation from thunderstorms and lightning with LOFT, ArXiv e-prints, 2015.

Meegan, C., Lichti, G., Bhat, P. N., Bissaldi, E., Briggs, M. S., Connaughton, V., Diehl, R., Fishman, G., Greiner, J., Hoover, A. S., van der Horst, A. J., von Kienlin, A., Kippen, R. M., Kouveliotou, C., McBreen, S., Paciesas, W. S., Preece, R., Steinle, H., Wallace, M. S., Wilson, R. B., and Wilson-Hodge, C.: The Fermi Gamma-ray Burst Monitor, apj, 702, 791-804, doi:10.1088/0004-637X/702/1/791, 2009.

Neubert, T., Kuvvetli, I., Budtz-Jørgensen, C., Østgaard, N., Reglero, V., and Arnold, N.: The atmosphere-space interactions monitor (ASIM) for the international space station, in: Proceedings of the ILWS Workshop, edited by Gopalswamy, N. and Bhattacharyya, A., p. 448, 2006.

Nisi, R. S., Østgaard, N., Gjesteland, T., and Collier, A. B.: An altitude and distance correction to the source fluence distribution of TGFs, Journal of Geophysical Research: Space Physics, 119, 8698–8704, doi:10.1002/2014JA019817, http://dx.doi.org/10.1002/2014JA019817, 2014.

Ostgaard, N., Gjesteland, T., Hansen, R. S., Collier, A. B., and Carlson, B.: The true fluence distribution of terrestrial gamma flashes at satellite altitude, Journal of Geophysical Research: Space Physics, 117, n/a–n/a, doi:10.1029/2011JA017365, http://dx.doi.org/10.1029/2011JA017365, 2012.

Ostgaard, N., Albrecthsen, K. H., Gjesteland, T., and Collier, A.: A new population of terrestrial gamma-ray flashes in the RHESSI data, Geophysical Research Letters, 42, 10,937–10,942, doi:10.1002/2015GL067064, http://dx.doi.org/10.1002/2015GL067064, 2015.

Sarria, D., Blelly, P.-L., and Forme, F.: MC-PEPTITA: a Monte Carlo model for Photon, Electron and Positron Tracking In Terrestrial Atmosphere. Application for a Terrestrial Gamma-ray Flash, Journal of Geophysical Research: Space Physics, pp. n/a–n/a, doi:10.1002/2014JA020695, http://dx.doi.org/10.1002/2014JA020695, 2014JA020695, 2015.

Sarria, D., Blelly, P.-L., Briggs, M. S., and Forme, F.: Studying the time histogram of a terrestrial electron beam detected from the opposite hemisphere of its associated TGF, Journal of Geophysical Research (Space Physics), 121, 4698–4704, doi:10.1002/2015JA021881, 2016.

Smith, D. M., Lin, R. P., Turin, P., Curtis, D. W., Primbsch, J. H., Campbell, R. D., Abiad, R., Schroeder, P., Cork, C. P., Hull, E. L., Landis, D. A., Madden, N. W., Malone, D., Pehl, R. H., Raudorf, T., Sangsingkeow, P., Boyle, R., Banks, I. S., Shirey, K., and Schwartz, R.: The RHESSI Spectrometer, solphys, 210, 33–60, doi:10.1023/A:1022400716414, 2002.

Smith, D. M., Lopez, L. I., Lin, R. P., and Barrington-Leigh, C. P.: Terrestrial Gamma-Ray Flashes Observed up to 20 MeV, Science, 307, 1085–1088, doi:10.1126/science.1107466, 2005.

Smith, D. M., Grefenstette, B. W., Splitt, M., Lazarus, S. M., Rassoul, H. K., Coleman, L. M., Dwyer, J. R., Lay, E. H., Holzworth, R. H., Cohen, M. B., Said, R., Inan, U. S., Chronis, T. G., and Takahashi, Y.: The Anomalous Terrestrial Gamma-ray Flash of 17 January 2004, AGU Fall Meeting Abstracts, p. A1040, 2006.

Surkov, V. V. and Hayakawa, M.: Underlying mechanisms of transient luminous events: a review, Annales Geophysicae, 30, 1185–1212, doi:10.5194/angeo-30-1185-2012, 2012.

Tavani, M., Barbiellini, G., Argan, A., Boffelli, F., Bulgarelli, A., Caraveo, P., Cattaneo, P. W., Chen, A. W., et al.: The AGILE Mission, aap, 502, 995–1013, doi:10.1051/0004-6361/200810527, 2009.

Ursi, A., Guidorzi, C., Marisaldi, M., Sarria, D., and Frontera, F.: Terrestrial gamma-ray flashes in the BeppoSAX data archive, Journal of Atmospheric and Solar-Terrestrial Physics, 156, 50–56, doi:10.1016/j.jastp.2017.02.014, 2017.

Voss, H. D., Imhof, W. L., Walt, M., Mobilia, J., Gaines, E. E., Reagan, J. B., Inan, U. S., Helliwell, R. A., Carpenter, D. L., and Katsufrakis, J. P.: Lightning-induced electron precipitation, Nature, 312, 740–742, doi:10.1038/312740a0, 1984.